ORIGINAL ARTICLE

Structural and mechanical evaluation of a new Ti-Nb-Mo alloy produced by high-energy ball milling with variable milling time for biomedical applications

Marwa Dahmani[1,2] · Mamoun Fellah[3,4] · Naouel Hezil[4,5] · Mohamed-Cherif Benoudia[1,2] · Mohammed Abdul Samad[6] · Alhanouf Alburaikan[7] · Hamiden Abd El-Wahed khalifa[7,8] · Aleksei Obrosov[9]

Abstract

The main focus of this work is to investigate the impact of varying milling times (2 to 18 h) on the structural and mechanical properties of the developed Ti-Nb-Mo alloy. The morphology, phase composition, microstructure, and mechanical behavior of milled and sintered Ti-25Nb-25Mo alloy samples were characterized systematically using x-ray diffraction, scanning electron microscope, optical microscope, and Vicker microhardness. It was noted that the quantity of the β-Ti phase increased as the milling time increased. After 12 h of milling, the synthesized alloys exhibited a spherical morphology and texture with homogeneous distribution. The milled alloys' structural evolution and morphological changes were found to be dependent on their milling duration. Morphological analysis revealed that the crystallite size and mean pore size decreased when the milling duration increased, reaching minimum values of 51 nm and < 1 μm, after 12 and 18 h respectively. As the milling time increased, the grain size decreased, resulting in an increase in density, microhardness, and elastic modulus. Ti-25Nb-25Mo will presents good anti-wear ability and higher resistance to plastic deformation due to enhanced mechanical characteristics (H/E, and H^3/E^2). Hence, the developed Ti-25Nb-25Mo alloys with reduced elastic modulus and desirable mechanical properties were found to be a promising option for biomedical applications.

Keywords Ti-25Nb-25Mo alloy · High-energy ball milling · Milling time · Structural evolution · Nanoparticle · Biomedical applications

✉ Marwa Dahmani
m.dahmani@ensti-annaba.dz

✉ Mamoun Fellah
mamoune.fellah@univ-khenchela.dz

✉ Aleksei Obrosov
aleksei.obrosov@b-tu.de

1 Department of Mining, Metallurgy and Materials Engineering, National Higher School of Technology and Engineering, 2000 Educational Places Sidi Amar, Annaba, Algeria

2 Laboratory of Mines, Metallurgy, and Materials (L3M), National Higher School of Technology and Engineering, 2000 Educational Places Sidi Amar, Annaba, Algeria

3 Mechanical Engineering Department, ABBES Laghrour-University, P.O 1252, 40004 Khenchela, Algeria

4 Biomaterial, Synthesis and Tribology Research Team, ABBES Laghrour-University, P.O 1252, 40004 Khenchela, Algeria

5 Matter Science Department, ABBES Laghrour-University, P.O 1252, 40004 Khenchela, Algeria

6 Mechanical Engineering Department and IRC-AM, King Fahd University of Petroleum & Minerals, 31261 Dhahran, KSA, Saudi Arabia

7 Department of Mathematics, College of Science and Arts, Qassim University, 51951 Al- Badaya, Saudi Arabia

8 Department of Operations and Management Research, Faculty of Graduate Studies of Statistical Research, Cairo University, Giza 12613, Egypt

9 Department of Physical Metallurgy and Materials Technology, Brandenburg Technical University, 03046 Cottbus, Germany

1 Introduction

Every year, approximately one million patients across the globe undergo surgery for total hip arthroplasty, which is considered to be one of the most significant advancements in the field of orthopedics [1, 2]. Total hip replacement refers to a surgical intervention to remove the damaged or injured cartilage and femoral head of the hip joint and replace it with an artificial hip prosthesis made of different synthetic materials. The primary goal of this surgery is to restore the normal functioning of the joint [3–5].

Although artificial hip joints are engineered to have a lifespan of 20 years, their longevity is often restricted due to issues such as biomechanical and biological incompatibility, as well as corrosion and wear-related problems that affect the stability of primary and secondary implants [1, 2, 4, 5]. Ongoing research and development efforts are focused on enhancing the design of hip prostheses, including the structures and materials employed, to lower the likelihood of failures and decrease the need for revision surgery [1, 6].

The biomedical materials domain is continually developing, with several unique alloy combinations emerging in the previous 20 years. Extensive research is being conducted, with a specific focus on titanium and its alloys owing to their exceptional mechanical and biological properties [7], such as outstanding resistance to corrosion in body fluid, remarkable strength, high biocompatibility, and good tribological characteristics. Moreover there are several straightforward methods that can possibly be used to improve their mechanical characteristics. Hence, titanium and its alloys have found widespread use as orthopedic implant materials and in medical industries [8–11].

Commercially pure titanium (cp-Ti) with different grades such as α-type, and its alloys (Ti–Al–Fe, and Ti–Al–Nb) such as α + β type, are presently the preferred choice for orthopedic implant materials because of their exceptional biocompatibility, resistance to corrosion, and an impressive ratio of strength to weight [12].

Although, as discussed by Niinomi et al. and Pengfei et al. [13, 14], Ti alloys have a higher Young modulus than human bone, these alloys may be biomechanically incompatible [12]. A difference in stiffness or elasticity between both the implant material and the hard tissues material, can lead to excessive stress-shielding effects during bone fixation and ultimately result in premature implant failure [15]. Besides that, some widely used Ti alloys (Ti–Al–Fe, Ti–Al–V) are susceptible to dangerous ion release, including Al or V [10]. The long-term in vivo implantation of such alloys has been associated with various problems, including Alzheimer's disease and mental disorders, due to the production of ions. As a result, there is a pressing need

for the creation of new titanium-based alloys that have low elasticity and containing metallic biocompatible elements such as Mo, Nb, Zr, Ta, and Sn [10, 16].

Ti-Nb-Zr, Ti-Mo-Zr-Fe, and Ti-Mo are among the most promising titanium alloys that have been authorized by the FDA [11]. Xu et al. [17], utilized XRD analysis to study the phase changes of the alloy and found that the Ti-35Zr-28Nb alloy was comprised of β-phase only. A similar result was reported in the works of Yan et al. [18], and Chui et al. [14]. β-type titanium-based alloys have caught the attention of researchers and industrialists for biomedical implant applications, thanks to their mechanical characteristics which closely resemble those of human bones. In their report, Fatichi et al. [19], found that the inclusion of 2 and 4 wt.% of zirconium in Ti-35Nb alloy is ideal for biomedical applications, as it hinders the generation of both α″ and ω phases which are responsible for an increase in elastic modulus. In [20], the stiffness of the Ti-Nb-Zr sample, which was milled and sintered, was reported to be 52 GPa, similar to the Young modulus of hard tissues. According to Li et al. [21], the content of the α-phase decreased, and the β-phase content increased with an increase in the Mo equivalent.

As a result, the yield strength of the Ti-Nb-Mo-Ta alloys decreased, while the strain at failure increased. In biomedical applications, Ti-10Mo-(3, 7, 10)Nb alloys are promising due to their combination of high strength and low elastic modulus. The equiaxed β-phase became the dominant phase when Mo and Nb were added [22]. Xu et al.′s research found that the Ti-Mo-Nb system exhibited higher values of Vickers microhardness, compression strength, and yield strength, along with high plastic strain and a reduced Young modulus (ranging from 24.7–28.4 GPa), which is an additional desirable property [22].

These alloys have the added benefit of improved corrosion resistance as they contain β-stabilizers, which are completely biocompatible elements. It was demonstrated by Dinu et al. [23], that the corrosion resistance of the ternary Ti-Nb-Zr system was superior when compared to the Ti-6Al-4 V alloy in all types of artificial human body environments. As mentioned by Lopes da Silva et al. [24], Ti alloys containing Nb and Zr demonstrated improved corrosion properties compared to pure titanium (cp-Ti). Neacsu et al."s in vitro research work has shown that the five newly developed low modulus alloy compositions, including Ti-12Mo, and Ti-(4, 6, 8, 10)Mo-(32, 24, 16, 8)Nb, exhibit favorable biocompatibility and do not adversely affect adhesion, morphology, and proliferation rate, in comparison to cp titanium [25].

Moreover, it is crucial for biomaterials to possess lower wear volume and coefficient of friction with high wear resistance to prevent the generation of wear debris and the liberation of metallic ions, which can potentially trigger undesirable bodily reactions [26]. According to Xu et al.

[10], Ti-35Zr-28Nb exhibits superior wear resistance compared to pure Ti and approaches that of Ti-6Al-4 V. The dominant wear mechanism of Ti-35Zr-28Nb is primarily abrasive wear, with adhesion wear also playing a role.

Furthermore, porous titanium-based alloys synthesized through mechanical alloying have become increasingly popular in the recent past. Mechanical alloying can be employed to generate a finer grain structure that exhibits enhanced mechanical properties. This technique can also obtain Ti- alloys with a lower Young modulus comparable to the hard tissues [27].

The milling time is a critical factor in the mechanical alloying process. As the milling duration is increased, the mechanical characteristics of the samples, including microhardness, density, compressive strength, and Young's modulus, were enhanced. In particular, elastic modulus of the Ti-Nb-Zr alloy sintered and milled for 4 h exhibited Young's modulus of 52 GPa, the same as the elastic modulus of hard tissue [20].

The milling duration was selected to attain a fine β-phase titanium structure [16]. Additionally, during the milling process, other elements such as Nb, Zr, Mo, and Mg were incorporated into the Ti structure, leading to a phase transformation to the titanium β phase [16]. These findings are comparable to the results of Gouvea et al. [28], who studied Ti-35Nb-5Mo samples that were ball-milled for 12, 24, 40, and 60 h, respectively. A study has been conducted to analyze the impact of alloying elements and milling duration on the microstructural changes in Ti-Nb alloy [29]. The XRD spectra indicated that the creation of a β-Ti solid solution happened after milling for more than 20 h [29].

As presented by Salvo et al. [29], the quantity of the β-Ti phase grew as the milling time increased, and the α-Ti phase was not detected at longer milling times. This structural change caused by milling time and chemical composition affected mechanical and tribological properties. Mendes et al. [30], mentioned that Ti-27Nb-13Zr alloy is categorized as α + β, and the formation of these phases is affected by the duration of milling. Prolonged milling time led to a rise in the α″ phase, which caused the alloys produced by powder milling for 2 and 6 h to have more β-Ti phase than α-Ti phase. When the milling time was extended to 10 h, an equiaxed structure with α-plates and α-colonies in the β matrix was observed, and all the Nb was in solution [30].

In the last few years, there has been a growing interest in new generation beta-type titanium alloys such as Ti-Nb, Ti-Mo, Ti-Nb-Mo, and Ti-Nb-Zr, their potential use as biomaterials, and the novel production procedure. The impact of Nb concentration on the structural and mechanical characteristics of Ti-Nb alloys was the aim of a work executed by Camposs-Quiros et al. [11]. Fellah et al. [31], also preformed a study on the improved physical and tribological properties of binary Ti–15Nb system for bone implant applications. Recently, several authors [12, 27, 32], have examined the effect of Mo content on different properties of Ti-xMo. The structural and

mechanical characteristics of biomedical Ti74xMoxNb26 β-alloys (×0, 2, 4, 6, and 8 at.%) with low modulus of elasticity were investigated by Li et al. [33]. Xu et al. and Gouvea et al. [22, 28], also reported research on ternary Ti-Nb-Mo alloy. Some significant researchers have successfully applied the same production principle in their studies, employing the powder metallurgy process especially high-energy ball milling to produce several beta-type titanium alloys with exceptional performance characteristics optimized for biomedical applications. Among the notable papers on this topic are those by researchers [16, 17, 21, 28, 34–37].

There are only a few studies dealing with alloys prepared by high energy ball milling process from pure elemental powders of Ti and other elements stabilizing the β-phase such as Nb, Mo and Zr for orthopedic application. As reported by Oshida et al. [38], Nb and Mo are elements that serve to stabilize the β-phase and lower the beta transition temperature. Nevertheless, Zr has long been recognized as a neutral element, and several studies have reported that its β-stabilizing impact on β-Ti alloy is primarily influenced by the existence of other alloying elements [39, 40].

Furthermore, most of the previous studies do not take into account the milling time effect on the microstructural, mechanical, and tribological behavior of mechanically alloyed and hot isostatically pressed Ti-25Nb-25Mo alloys. Ti, Nb, and Mo are biocompatible metals that are non-toxic and non-allergenic. Incorporating Nb and Mo into Ti favored the mechanical biocompatibility of the alloys with human bone [25, 41–43]. Hence, the aim of this paper is to create beta type titanium-based alloys with new chemical composition and to investigate milling process effect on the structural evolution, and mechanical behavior of the Ti-25Nb-25Mo system.

2 Experimental methods

2.1 Sample preparation

The sample preparation was initiated by acquiring pure elemental powders of commercially available Ti, Nb, and Mo, whose properties and chemical constituents are shown in Table 1. Precision balance was used to weigh the starting powders. The weight composition of Ti-25Nb-25Mo samples was achieved via mechanical alloying (MA) process by milling elemental powders for various periods of 2, 6, 12, and 18 h respectively, in a Fritsch Pulverisette P7 high-energy ball mill at ambient temperature in an argon environment to prevent oxidation. An agate vial, 80 ml in volume and agate balls of 10 mm diameter with the weight of balls being 10 times greater than that of powder were used at a rotational speed of 400 rpm. Milling cycles of 15 min were employed in the synthesis process, combined with rest periods of 5 min to prevent excessive heating inside the vials.

Table 1 Chemical constituents and properties of as-received powders [14, 28, 44]

Characteristic	Ti	Nb	Mo
Purity	> 99.9%		
Particle size	< 100 μm		
Atomic radius (nm)	0.147	0.143	0.140
Phase at STP	Solid		
Crystal system	(hcp)	(bcc)	(bcc)
Melting temperature (°C)	1941	2469	2623
Particle form	The particles are irregular in shape		
Density (g/cm³)	4.5	8.35	10.22
Fabrication process	Chemical process		

Subsequently, the pre-alloyed powders were subjected to a powder metallurgy procedure using both cold and hot pressing. During cold pressing, the mechanically alloyed powders were loaded into the rigid steel die and uniaxially compressed at a pressure of 230 MPa using a manual hydraulic press (Specac 25 Ton), forming a cylindrical shape with a diameter of 13 mm diameter and a thickness of 4 mm.

After the cold pressing step, the specimens were processed by hot isostatic pressing (HIPed) at a temperature of 1050 °C and a pressure of 100 MPa, with 30 min of holding time [21, 45].

The HIPed specimens were subsequently sintered using a vacuum furnace (Nabertherm GmbH, Germany) at a sintering temperature of 1250 °C for a dwell time of 3 h under a pressure of 10^{-8} MPa. In order to avoid oxidation during the sintering process, the specimens were enclosed within the vacuum-sealed quartz tubes. The conditions of heat treatment were selected to attain high density and closed porosity [34]. The furnace was used to gradually cool the sintered samples to room temperature. Figure 1 demonstrates the hot pressing and the sintering cycles of the pellets.

The scanning electron microscopic images of pure Ti, Nb, and Mo powders used in the mechanical alloying process are displayed in Fig. 2. The powder of Ti shows irregularly shaped particles with the largest size of about 60 μm. The Nb powder particles demonstrated a triangular form with an average size of around 80 μm, along with smaller dimension particles of less than 8 μm. The Mo powder particles had a porous spongy-textured irregular shape with a mixture of two major dimensions, one smaller than 20 μm and the other smaller than 1 μm.

The creation of a nanostructured compound can be broken down into three stages: synthesis of the crystalline phase in the powder form, the forming stage, and heat treatment at high temperature, called sintering [46]. Figure 3 shows the steps of sample production.

2.2 Materials characterizations

2.2.1 Structural characterizations

X-ray diffraction (XRD), scanning electron microscopy (SEM), and optical microscopic (OM) analysis were used to examine the samples' microstructural features, phase transformation, changes in crystallite size, micro-strain, lattice parameter, particle size, pore size distribution, shape and morphology of powders during ball milling.

The morphology, porosity, and mean pore size of starting, milled, and consolidated specimens were observed and measured using a SEM (FEI-Quanta 250, USA). The EDS analysis was employed to estimate the quantitative analysis of elemental chemical composition (EDAX TEAM, Czech Republic).

The consolidated Ti-25Nb-25Mo specimens' microstructure was determined and verified through optical microscopy (OM) (Nikon, ECLIPSE LV 150N, JAPAN). Fourier transform infrared spectroscopy (FTIR) was used to examine the absorption bands. The analysis was conducted using a SHIMADZU IR Spirit-T instrument from Japan, covering a range of 145 to 4000 cm⁻¹.

The phase of the mixed, milled and sintered Ti-25Nb-25Mo was investigated using diffractometer (XRD; Eco D8 ADVANCE, BRUKER, 20 mA, 40 kV), with copper anode ($\lambda_{Cu} = 1.5418$ A°). The measurement was carried out in 2Θ range from 20 to 90° in increments of 0.02°, with each measurement taken at intervals of 1 s. The XRD profiles were

Fig. 1 Heat treatment cycles of the milled and compacted Ti25Nb25Mo samples for: **a**) hot pressing, and **b**) sintering process
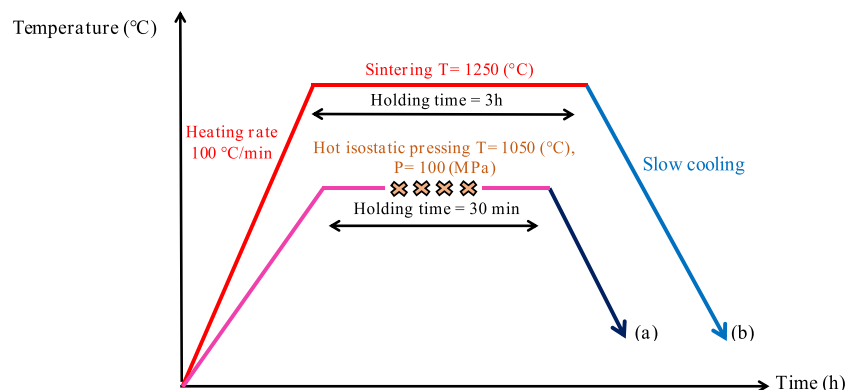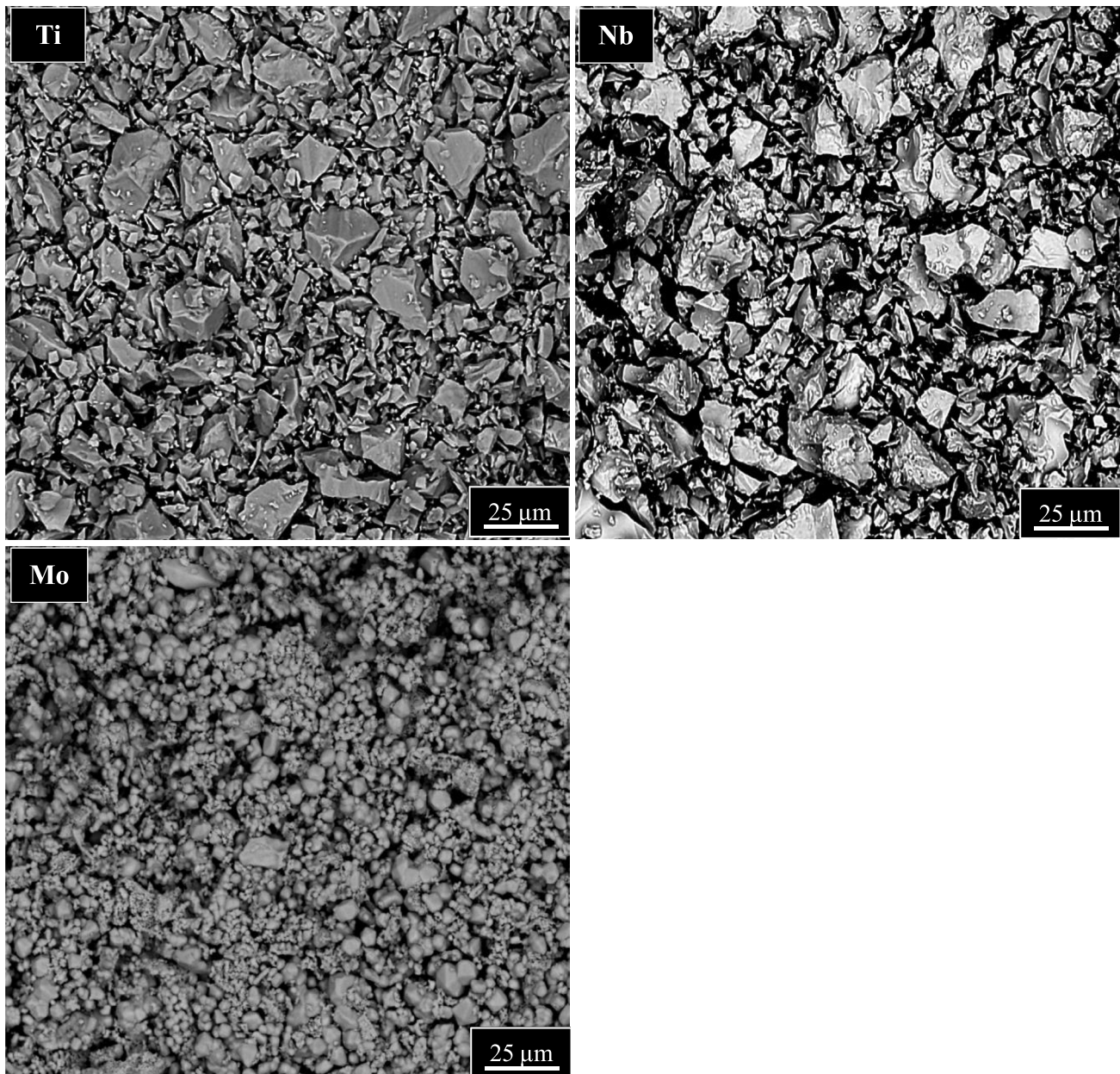
Fig. 2 SEM microphotographs of starting pure powders (Ti, Nb, and Mo)

thoroughly examined, and crystallographic parameters such as lattice parameter, crystallite size, and lattice distortion were calculated. The microstrain, and crystallite size of the milled powders were deduced and verified through the use of Scherrer [31, 47], and Williamson–Hall [48] equations, respectively.

$$D = \frac{0.9\,\lambda}{\beta\,\cos\theta} \qquad (1)$$

$$\beta\,\cos\theta = \frac{0.9\,\lambda}{D} + 4\varepsilon\,\sin\theta \qquad (2)$$

where β represents the full width at half maximum (FWHM), θ is the incident glancing angle, ε is the lattice strain, K is the form factor (~0.94), λ is the wavelength of the incident wave, and D is the crystallite size.

2.2.2 Physical and Mechanical ccharacterizations

The Archimedes approach was employed to calculate the density of heat treated samples [26, 49]. The Young's modulus and the microhardness of HIPed and sintered Ti-25Nb-25Mo alloys were determined by the instrumented
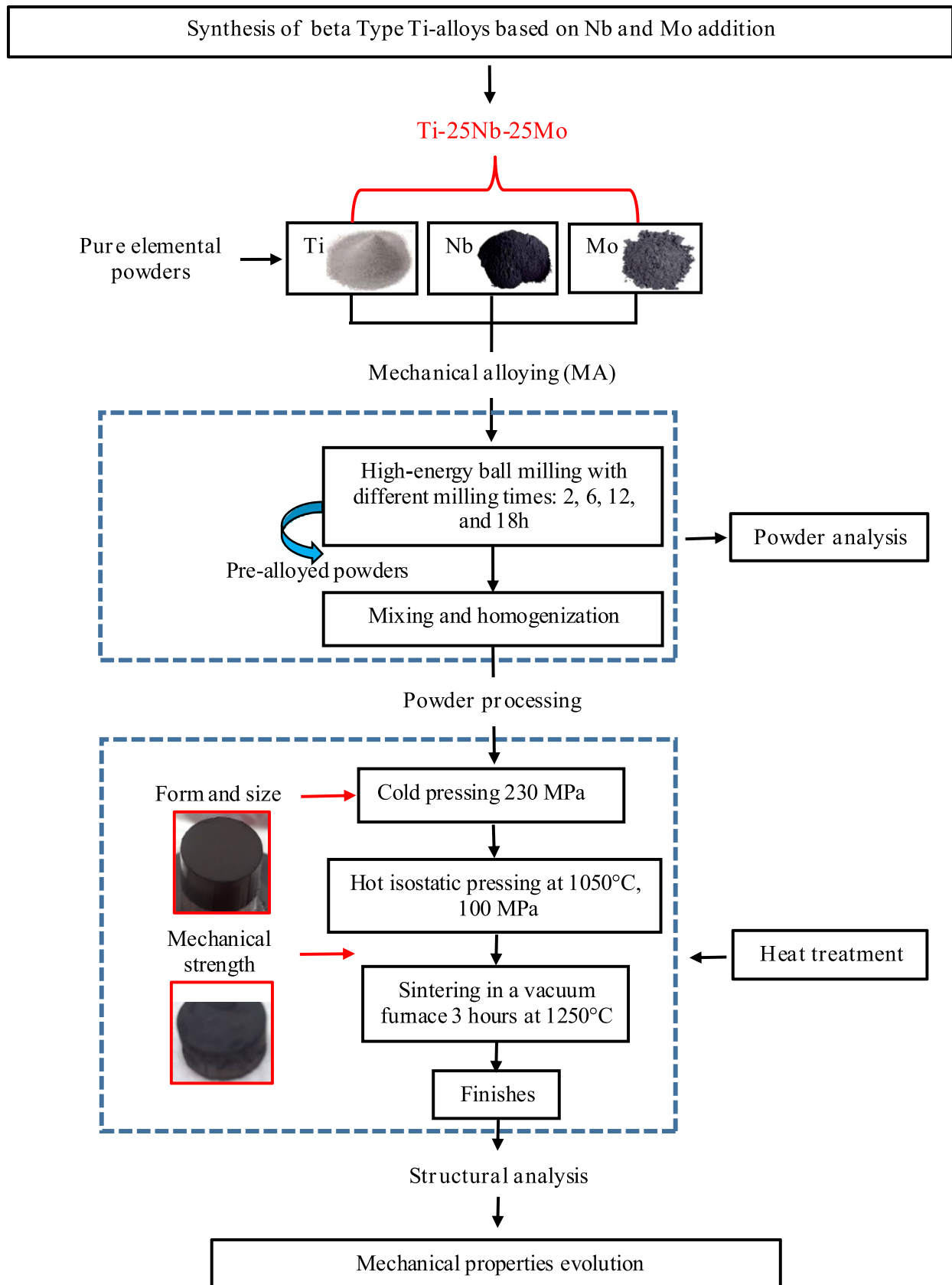
Fig. 3 Samples production process and characterization methods of Ti25Nb25Mo alloys

micro-indentation (Zwick/Roell, ZHU 2.5, Germany) with a Vickers diamond indenter by applying an indent load of 500 gf ($HV_{0.5}$) for a duration of 10 s at room temperature. During the measurement, a distance of at least three times the size of the indent was maintained between any two indents, while five measurements were recorded for each sample.

A Cyber TECHNOLOGIES CT 100 (GmbH, Germany) laser source profilometer was utilized for measuring the surface roughness parameters of the compacted and sintered specimens to determine the average roughness (Ra). The ISO 4287 standard was used to calculate the mean average surface roughness (Ra) [50].

3 Results and discussion

3.1 Microstructural evolution

3.1.1 Morphology and microstructure of pre-alloyed powders

Figure 4 represents the morphology of Ti-25Nb-25Mo powder after mechanical alloying with varying milling times: a) 2 h, b) 6 h, c) 12 h, and d) 18 h, respectively. The size of the powder particles produced by ball milling increased initially and then decreased, which corresponds to the common features of the mechanical alloying method [35].

The microphotographs show particle size distribution and agglomerate structure, indicating that the original substrate powders underwent continuous cold welding and fracturing. The majority of the agglomerated rounded particles range in size from 1 to 10 μm [27]. The milled powder was observed to be comprised of many nanoparticles, that might be attributed to the repeated collisions of the balls and extrusion, resulting in the metal powder being continuously plasticized, hardened, cold-welded, and broken [35].

After 2 h of milling (Fig. 4a), the powder charge contained a minimum of 15 percent by volume of the alloy ductile phase that functioned as a binding agent. In this stage, the average particle size s between 5 and 10 μm. The plastic deformation of the powder particles caused by the impact force results in hardening and fracturing [51]. The newly created surfaces allow the particles to join together, resulting in an increase in particle size (10 μm in our work) [51]. For the samples milled at 6 and 12 h (Fig. 4b, and c) respectively, the deformation persists and the particles undergo hardening and eventually fracture due to the fatigue mechanism. The fragments produced through this mechanism have the ability to further decrease in size to achieve the nanometric dimensions, as all the particles presented less than 1 μm, which can be clearly seen in Fig. 4b, c, and d, when there are no significant agglomeration dynamics [32, 46]. During this step, the tendency to fracture prevails instead of cold welding. The particle structure is constantly being refined due to the incessant impact of the grinding bodies, but the particle size remains unchanged [32]. As a result, there is a reduction in interlamellar distances and the percentage of lamellar structures within each particle increases [46].

Following a specific period of milling, an equilibrium state is attained in which the welding rate, aimed at augmenting the mean particle size, balances with the fracture rate, intended to diminish the mean powder particle size of the compound [29, 32]. Particles of a smaller size can resist deformation without breaking and have a tendency to weld together to form larger parts, forming intermediate-sized particles [29, 32, 46, 51].

At this point (18 h of milling Fig. 4 d), the range of particle sizes is limited due to the fact that larger particles tend to break down into smaller ones while smaller fragments have a tendency to agglomerate together and increase in size to revert to the micrometer scale (1 and 3 μm), as shown in Fig. 4d. The interlamellar distance becomes small in a few minutes, and the size of the crystallites (or grains) is refined until they achieve nanometric dimensions [51].

The amount of time required to form a particular structure within a system is determined by various factors including the initial particle size and properties of the constituents, the equipment utilized, and the operational settings of the equipment. Although, when the initial particle size is relatively large, the rate of internal structure refinement including particle size, crystallite size, etc., has an approximately logarithmic dependence on processing time [51].

As demonstrated by Salvo et al. [29], the longer milling time in Ti-Nb-based alloys produced both texturing and spherical morphology of the synthesized samples. During high-energy ball milling, texture formation is a significant phenomenon characterized by the development of preferred crystallographic orientations in the material. As milling time increases, the material undergoes severe plastic deformation due to the cumulative impact of high-energy collisions. This deformation causes the material's crystallographic orientations to align along specific directions or planes, marking the initial stages of texture formation. At longer milling times, the mechanical deformation becomes even more pronounced, leading to further alignment of crystallographic planes. The material may exhibit a well-defined texture with preferred orientations along specific crystallographic axes. The transformation of particles into spherical shapes is a result of the minimization of Gibbs's free energy values in powder particles that occurs during the milling process [29]. Compared to the original powders, the distribution of powder particle sizes becomes relatively uniform after extended milling durations.

The energy-dispersive spectroscopy analysis (Fig. 5) demonstrated that there was a rise in the concentration of contaminants as the milling time increased.
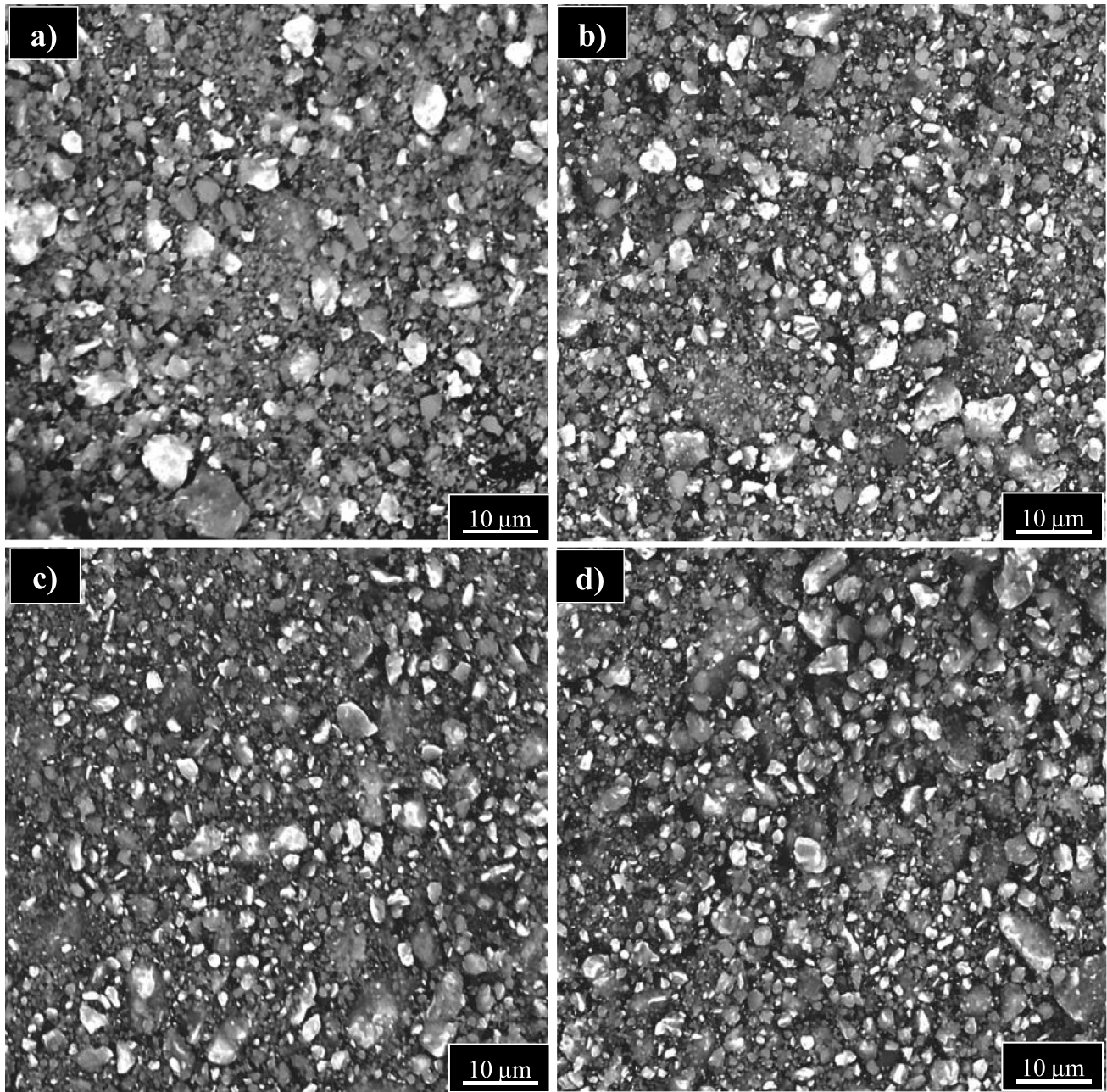
Fig. 4 SEM micrographs of Ti-25Nb-25Mo pre-alloyed powders after milling process at different milling time: **a**) 2 h, **b**) 6 h, **c**) 12 h, and **d**) 18 h

Figure 5 shows the EDS analysis of Ti-25Nb-25Mo for 2, 6, 12, and 18 h of milling time. After a 2 and 6-h milling period, we can only see the alloy composition (Ti, Nb, and Mo) with little silicone and no contamination elements (Fig. 5a, b), but for alloys milled for 6, 12, and 18 h, the EDS analysis showed the presence of silicon, oxygen and nitrogen from the atmosphere, agate balls, and vials. (Fig. 5c, d).

Hence, the primary source of contamination appears to be SiO_2 from the agate material. Moreover, the presence of a significant amount of oxygen may be explained by uncertainty

of the EDS analysis results, or can be also described as the inability to maintain a controlled atmosphere inside the vials during the milling process due to the limited capabilities in our laboratories. The qualitative analysis indicated that the concentration of contaminants increased with longer milling times. Furthermore, EDS/SEM mapping revealed that Ti, Nb, and Mo, along with Si, O, and N contaminants, were uniformly distributed, as shown in Fig. 6.

Previous research has documented that the container material can contaminate the powder as a result of the effect of
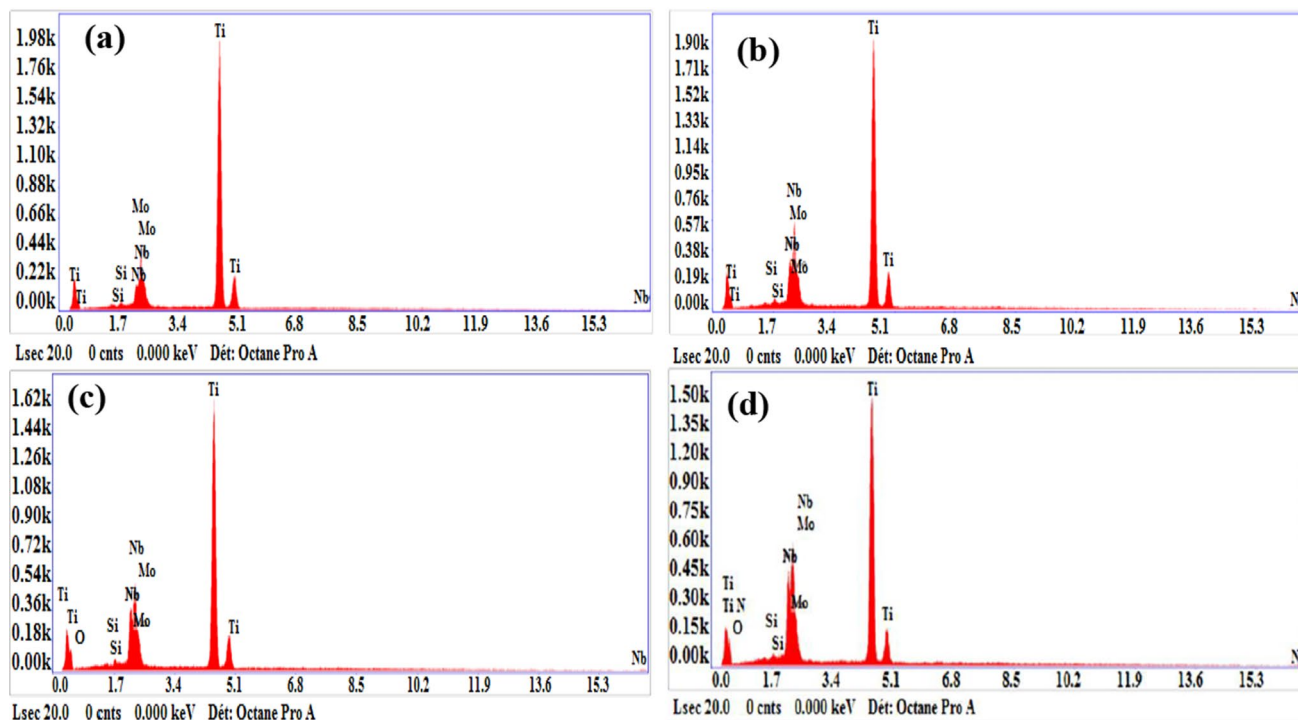
Fig. 5 EDS analysis of Ti-25Nb-25Mo powders milled for: **a**) 2 h, **b**) 6 h, **c**) 12 h, and 18 h

grinding media against the container walls. This occurs because the material from the container can detach and mix with the powder, leading to alterations in its chemical composition [51–54]. The amounts of chemical elements in pre-alloyed Ti-25Nb-25Mo samples are presented in Table 2.

The Ti-alloy with a high concentration of β-stabilizing elements (25 at.% Nb, and 25 at.% Mo) exhibit only β-phase with different chemical constituent (β-Ti, β-Nb, and β-Mo) as presented in Fig. 7, due to the high Mo equivalent value which is calculated using the following equation [35]:

$$[Mo]_{eq} = Mo + \frac{Nb}{3.6} + \frac{Ta}{4.5} + \frac{W}{2} + \frac{Cr}{O}.65 + \frac{V}{1} + \frac{Fe}{0.35} + \frac{Ni}{0.8} = 31.9\%$$

(3)

At a composition of 25 (at.%) for both Nb and Mo elements, the Ti-Nb-Mo system forms an alloy with a distinct structure predominantly composed of the Ti-β phase. However, this structure also includes insoluble elements such as Mo and Nb. These findings are substantiated by the ternary diagram of the Ti-Nb-Mo system, which was obtained at a temperature of 1100 °C [55], as depicted in Fig. 8.

3.1.2 IR analysis of pre-alloyed powders

Figure 9 displays the FTIR spectra corresponding to the milled powders at various milling durations (2–18 h).

The spectrum exhibits bands indicative of the stretching vibrations of O–H groups (approximately 3200–3670 cm^{-1}), along with bending vibrations in H$_2$O molecules (around 2000 cm^{-1}). Moreover, the IR profiles unveiled the existence of amine groups N–H (3100–3500 cm^{-1}), Si–H (2100–2360 cm^{-1}), and Si–O (1000–1100 cm^{-1}) [56, 57]. The peaks of these components present a lower percentage of transmittance compared to the peaks of metallic oxide bonds, which indicate the presence of trace amounts of these elements in the Ti-25Nb-25Mo samples. These results are well corroborated with the EDS analysis.

The existence of oxygen and nitrogen can be attributed to the atmosphere's contamination and the silicon from the agate balls and vials, while the primary source of hydrogen is the raw Ti powder. Based on Fig. 9, it can be observed that the bands related to Ti–O vibration bonds appear within the frequency ranges of 150–450 cm^{-1}. *Craver. D.C* [56], stated that the bonds of TiO$_2$ occur at 200–450 cm^{-1} and 450-900 cm^{-1}.

In our research, the vibration bands between oxygen and metal (O-M–O) exhibit a range of 145 to 500 cm^{-1}. Previous studies have shown that the vibration bands of Nb and Mo oxides are observed as M–O (Mo–O at 850 cm^{-1}, Nb–O at 880 cm^{-1}) and M–O-M (Mo–O-Mo at 500 cm^{-1}, Nb–O-Nb at 650 and 780 cm^{-1}). Additionally, NbO$_6$ shows a vibration band at 820 cm^{-1}, while Nb$_2$O$_5$ displays a range of 400 to 1100 cm^{-1} [58–60].

3.1.3 XRD analysis of Ti-25Nb-25Mo powders

Figure 10 presents the XRD patterns of pure elemental powders of Ti, Nb, and Mo (Fig. 10a), and Ti-25Nb-25Mo
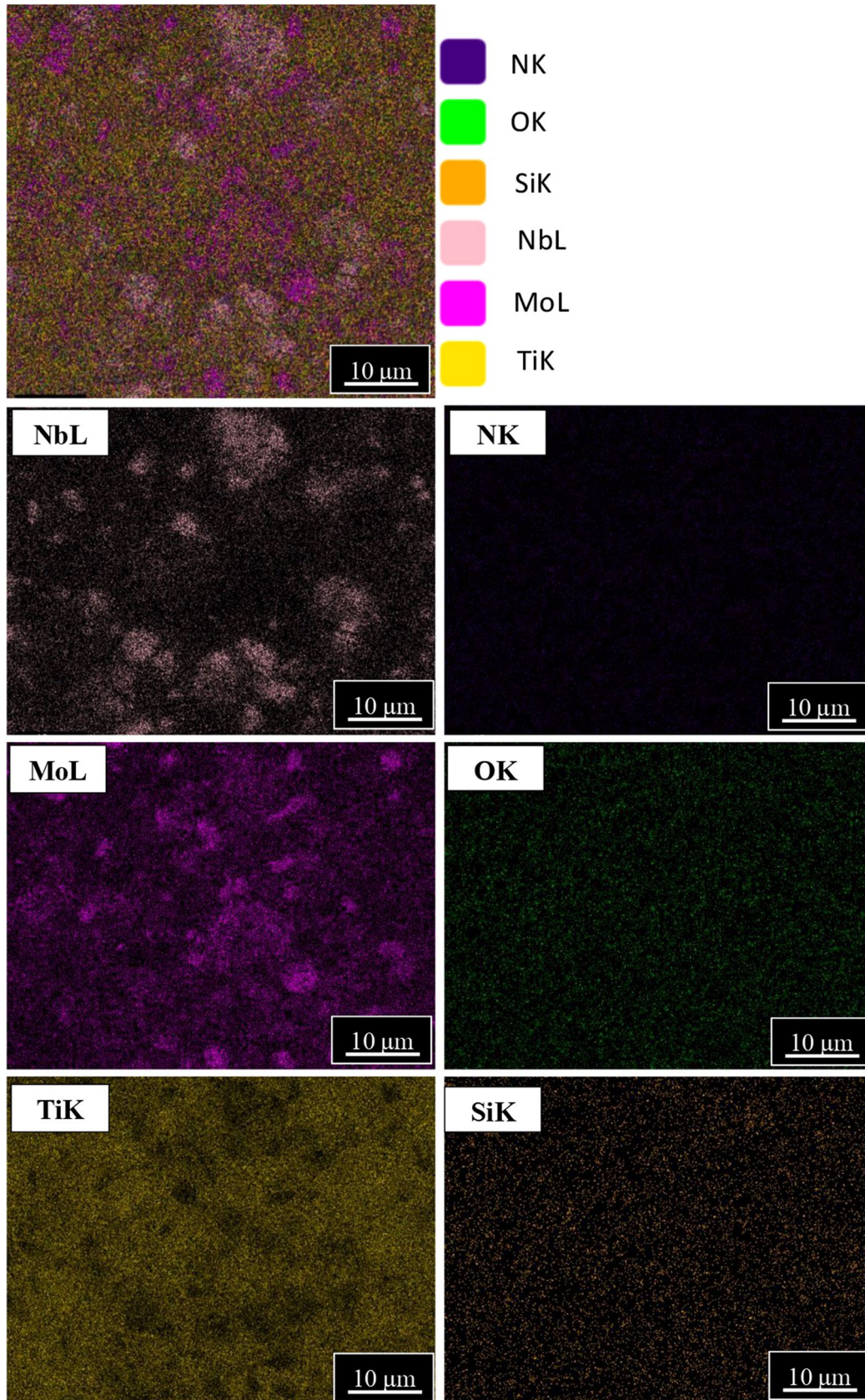
Fig. 6 EDS analysis map of based and contaminated chemical elements distribution in Ti-25Nb-25Mo powders milled at 18 h

Table 2 Quantitative analysis (EDS) results of Ti-25Nb-25Mo powders subjected to different milling durations (2–18 h)

Elements (at. %)	O	N	Si	Ti	Nb	Mo
2 h	-	-	2.31	55.52	18.13	24.04
6 h	-	-	2.60	51.87	20.1	25.43
12 h	13.93	-	1.99	46.41	16.89	19.78
18 h	15.26	5.16	1.73	36.72	19.35	21.73
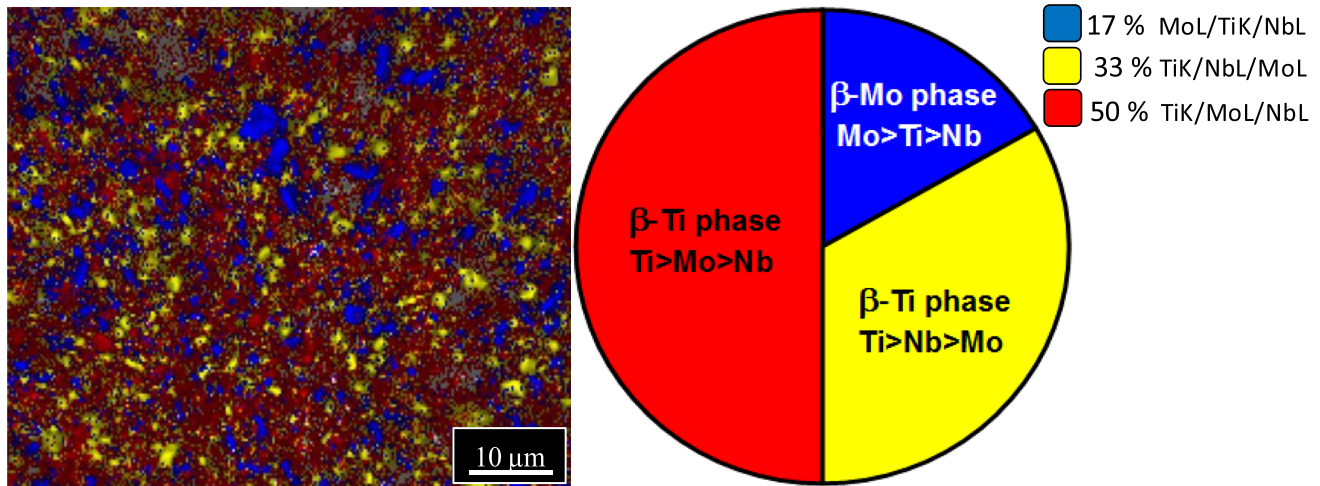
Fig. 7 EDS mapping of phase distribution in pre-alloyed Ti-25Nb-25Mo powders milled at 18 h

powder after the milling process with varying milling times (2–18 h) (Fig. 10b). It is evident from Fig. 10b that, as milling time increases from 2 to 18 h, there was a reduction in peak intensity, and the peaks become wider. The XRD pattern of the Ti-25Nb-25Mo powder in its initial state exhibits diffraction peaks that correspond to Ti, Nb, and Mo, and the characteristic (hkl) lines of these elements become visible only after 15 min of milling process [14, 18].

The peaks with the highest intensity for Mo at orientations (110) and (211) are observed at 2θ angles of 40.58° and 73.98° respectively. Similarly, for Nb, the most prominent reflections for orientations (110) and (211) are detected at 2θ angles of 38.48° and 69.59° respectively, as presented in Fig. 10a.

After 2 h of milling, distinct peaks corresponding to the elements Ti, and Nb were visible. However, the peak for Mo disappeared, suggesting that mechanical alloying resulted in the creation of a metastable solid solution, β-phase at orientations (110), (200), (211), and (220) in place of Mo.

In the initial stage of mechanical alloying, the elements blended to form a homogeneous mixture. The intensity of the Ti peaks decreased with time, whereas the Nb peaks increased. Following a milling time of 6 h, there was no visible peak observed in the XRD pattern that corresponded to (101), (102), (103), and (004) α-Ti. However the intensity of the peak corresponding to (100) α-Ti decreased with increasing milling time. The Nb peaks were located in close proximity to those of β-Ti on the diffractograms at orientations (110), and their intensity appeared to decrease slowly [16].

Gouvea et al. [35], also noted a similar trend through their XRD analysis. Based on our XRD patterns, it was observed that the formation of β-Ti solid solution took place after a milling duration of 2 h due to the high value
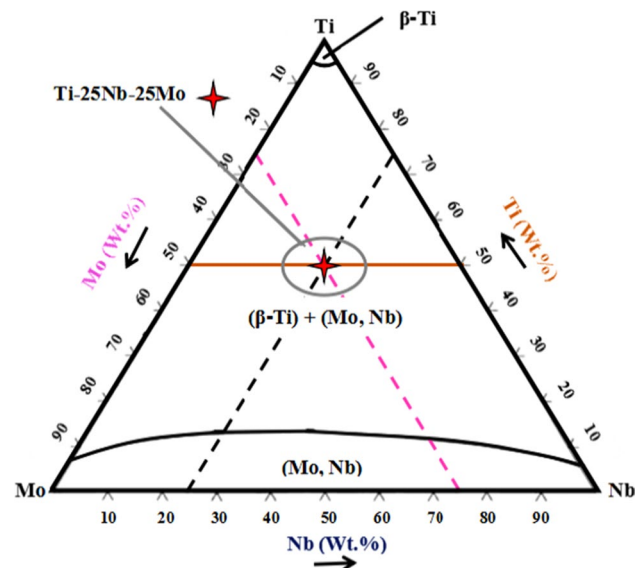

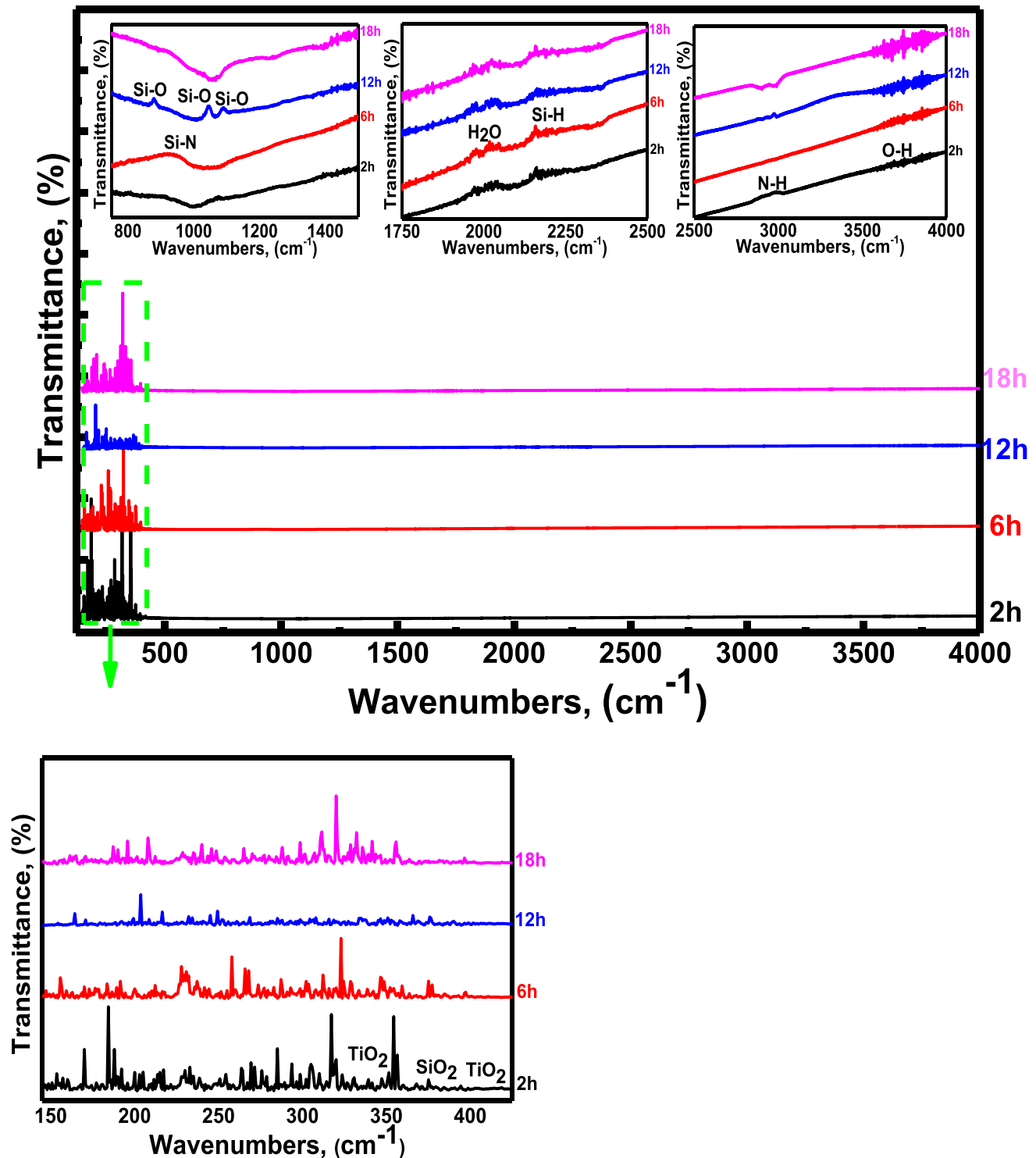**Fig. 8** Ternary phase diagram of Ti-25Nb-25Mo system (isothermal section at 1100 °C) [55]

Fig. 9 IR profiles of pre-alloyed Ti-25Nb-25Mo powders milled at varying times (2, 6, 12, and 18 h)

of Mo equivalent ([Mo]$_{eq}$ = 31.9 Wt. % as calculated by (Eq. 3)). The details of the impact of Mo$_{eq}$ on the phase transformation were discussed in [21]. As the milling time was increased, the proportion of the β-Ti phase also increased, particularly at longer milling durations. A comparable finding was documented in other works, such as, Yan et al. [18], for the Ti-Nb-Zr alloy, Chui et al. [14], for Ti-Zr–Nb-Mo system, Kalita et al. [37], on Ti-Nb alloy with Mo, and Ta addition, and Li et al. [45] on Ti-Nb-Mo samples.
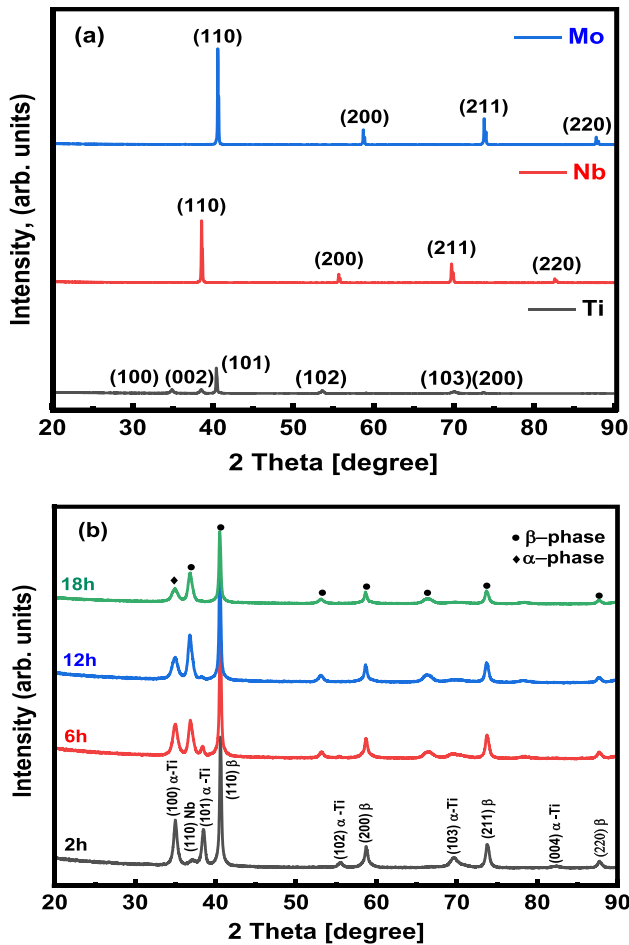
Fig. 10 XRD patterns of: **a**) initial pure particles powder of Ti, Nb, and Mo, **b**) pre-alloyed powders of Ti-25Nb-25Mo after mechanical alloying process as function of milling times of 2, 6, 12, and 18 h

3.1.4 Lattice parameter evolution, mean crystallite size, and micro-strain

Lattice parameter {a_β} The β-phase lattice parameter (a_β) was estimated using the XRD patterns. Figure 11 depicts the evolution of Ti-25Nb-25Mo lattice parameters $<a_\beta>$ (Å) for different milling time. The a_β increases from 3.144 to 3.150 Å as milling time increases from 2 to 18 h, respectively.

When Mo and Nb were introduced, the equiaxed β-phase became the dominant phase [22]. The Ti-25Nb-25Mo alloy with a milling time of 18 h has the highest lattice parameter due to the plastique deformation of powder particles resulting in several types of imperfections including stacking faults, vacancies, and dislocations. In addition, the presence of 25 (at.%) Mo content into Ti-25Nb introduces higher lattice distortions [61], which leads to the β phase's lattice parameter increase, because the atomic radius of Mo is smaller (0.139 nm) than that of Nb (0.143 nm) and Ti (0.147 nm) [14]. Combining with the Bragg diffraction formula of:
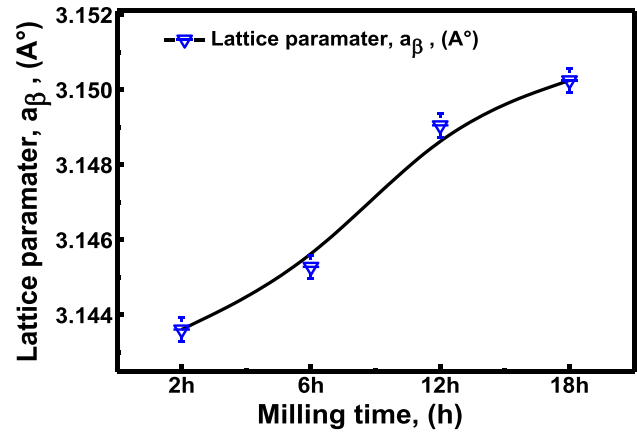

Fig. 11 Lattice parameter $<a_\beta>$ (Å) evolution of pre-alloyed Ti-25Nb-25Mo specimens as function of milling times (2–18 h)

$$2d \sin\theta = \lambda \tag{4}$$

The lattice parameter (a_β) may be expressed in the following form [18]:

$$a_\beta = \frac{\lambda\sqrt{h^2 + k^2 + l^2}}{2\sin\theta} \tag{5}$$

As depicted in Fig. 12, the Bragg angle demonstrates a shift towards a lower value for the specimens (milled at 6, 12, and 18 h), suggesting a slight increase in the lattice parameter.

Mean crystallite size {D}, and micro-strain {ε} Figure 13 illustrates the mean crystallite size and lattice strain evolution of Ti-25Nb-25Mo, respectively during various milling times (2–18 h). The average crystallite size reduced from 62 to 41 nm as milling time increased from 2 to 18 h.
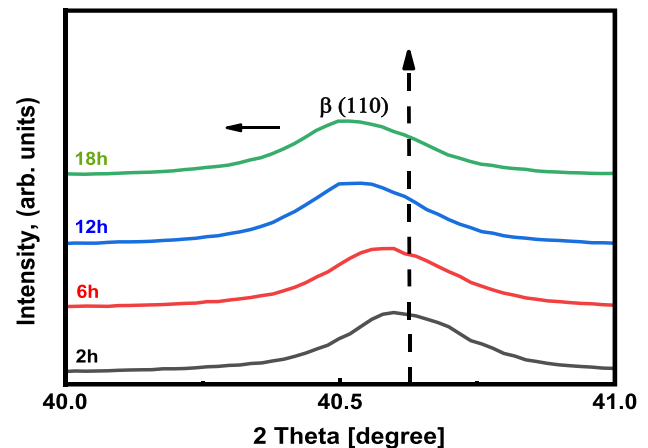

Fig. 12 XRD patterns amplification, indicating a shift of the peaks towards lower angles (2Θ) of Ti-25Nb-25Mo after mechanical alloying process for: 2, 6, 12, and 18 h
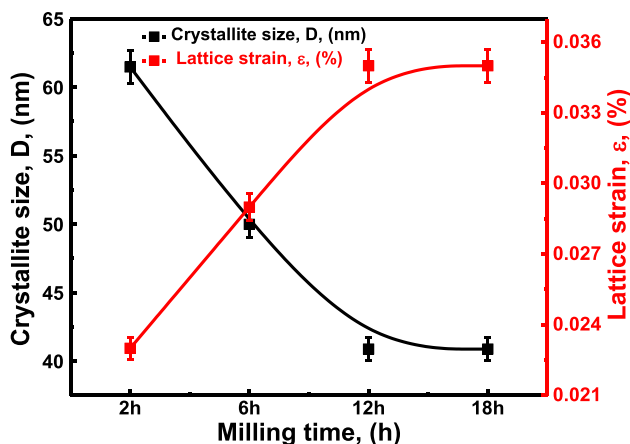
Fig. 13 Mean crystallite size, (nm) and lattice strain, (%) variation of pre-alloyed Ti-25Nb-25Mo specimens' mixture at various milling times (2, 6, 12, and 18 h)

The changes described above may be attributed to the mechanical energy transferred during the milling process, which is significant enough to cause plastic deformation of the three constituent powders of Ti, Nb, and Mo [62].

During the milling period of 12 to 18 h, the dependence of crystallite size on milling time decreased. In this stage, the reduction in size was slower, reaching a value of approximately 41 nm, which is a lower rate compared to the initial milling stage. The primary cause of the decrease in crystallite size is the intense plastic deformation of the powder during the milling process. With ongoing deformation, the particles undergo hardening and fracture via fatigue-based mechanisms. In cases where substantial agglomeration forces are not present, the fragments created by this mechanism can continue to decrease in dimensions [32, 46].

The continuous action of the grinding bodies leads to a continuous refinement of the particle structure, but the particle size remains constant. This process results in a reduction of interlamellar spacing and the lamellar structure count present in each nanoparticle increases [29, 32, 46, 51].

The interlamellar distance decreases over time, and the size of the crystallites is refined to nanometric dimensions [51]. Another explanation is that higher defect densities increase the possibility of nucleation sites during crystallization [62].

The changes in the obtained microstrain {ε} are also recorded as a function of milling time in Fig. 13. A significant increase in microstrain can be observed in the initial milling phase of 2 to 6 h, reaching 0.029%. Subsequently, for the milling period from 12 to 18 h, the microstrain further increases to 0.035%. The observed outcomes can be related to the impact of mechanical energy during the grinding process, which is capable of inducing plastic deformation of Ti, Nb, and Mo elemental powders.

After 12, and 18 h of milling, we can see a significant increase in microstrain up to 0.035%. This could be due to a high density of dislocation and a high concentration of stacking defects [62]. Mechanical alloying leads to the transfer of high energy to the base powders, which in turn causes a substantial density of defects, particularly dislocations [45]. The powders are almost amorphous after 48 h of mechanical alloying. This has been reported also by Sochacka et al. [27]. Some researchers confirmed that an increase in microstrain can be related to a decrease in crystallite size, which is consistent with the current work (Fig. 13) [61, 63].

Figure 14 depicts the Williamson-Hall plots of the Ti-25Nb-25Mo alloy after undergoing various milling durations. The experimental data points are represented by symbols, while the solid lines represent the fitted data obtained from the analysis. The slope of the linear regression line corresponds to the microstrain ε.

These plots provide valuable insights into the crystallite size and lattice strain of the Ti-25Nb-25Mo alloy with varying milling periods. By examining the plots, you can observe the trends and patterns in the experimental data, as well as the accuracy of the fitting performed using the Williamson-Hall equation (Eq. 2). The slope of the fitted data showed a decrease from 0.0019 to 0.0009 after 2 and 6 h, respectively. Subsequently, it exhibited an increase to 0.00098 and 0.001 at 18 and 12 h, respectively.

3.2 Structural, physical, and mechanical performance of consolidated samples

3.2.1 Relative porosity and density measurements

Figure 15 shows the relative porosity and relative density (%) of the sintered samples with varying milling times. The relative porosity of milled and sintered samples decreased from 22 to 18% as milling time increased. Conversely, as can be seen that the Ti–25Nb–25Mo alloy's relative density (%) increased as the milling time increased. The sample milled at 12 h had the highest sintered density of 82% and a relative porosity of 18%.

These results were obtained due to a decrease in pore size due to the predominance of particle fracture in the cold welding process [51], an increase in closed porosity, and a decrease in open porosity [33]. In addition, the powder particles were smaller and more uniform in size than the starting powders. Due to cold welding-induced particle agglomeration, the density decreases to 79.55% after 18 h of milling, resulting in an increase in grain size, porosity, and pore size.

As mentioned by Xu et al. [17], Ti alloy with high β stabilizing elements concentration was reported to have achieved near-complete density with no observable pores. They also displayed uniform microstructures consisting of a single β
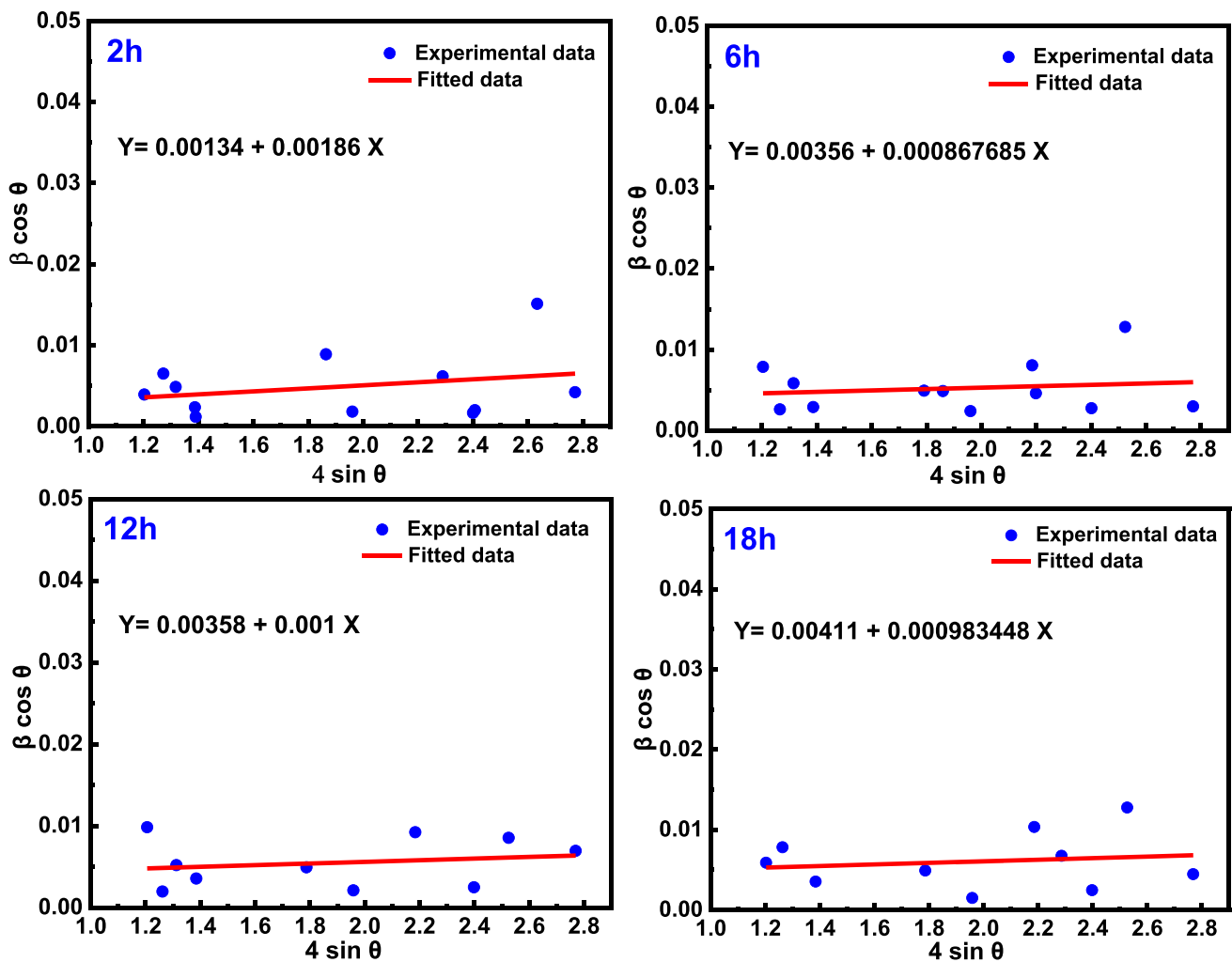
Fig. 14 Williamson–Hall Plots of pre-alloyed Ti-25Nb-25Mo alloy after various milling times from 2 to 18 h

phase, and high relative density was attained through sintering pre-alloyed powder at 1550 ℃.

The porosity level in nanomaterials is highly dependent on the mechanically alloyed specimens' processing technique. The pore size can be smaller than or equal to the grain size even after agglomeration. The mechanical properties of nanomaterials can be greatly influenced by porosity and mean pore size [64].

3.2.2 Porosity and pore distribution

Figure 16 represents the variation of porosity and pore size distribution of Ti-25Nb-25Mo with milling time. Pore size was reduced to less than 100 μm due to the cold-welding process's dominance of particle fracture. In addition, the particles were smaller and more uniform in size than the starting powders [20]. In contrast to the first stage, at 12 h of milling the majority of powders' porosity decreased to
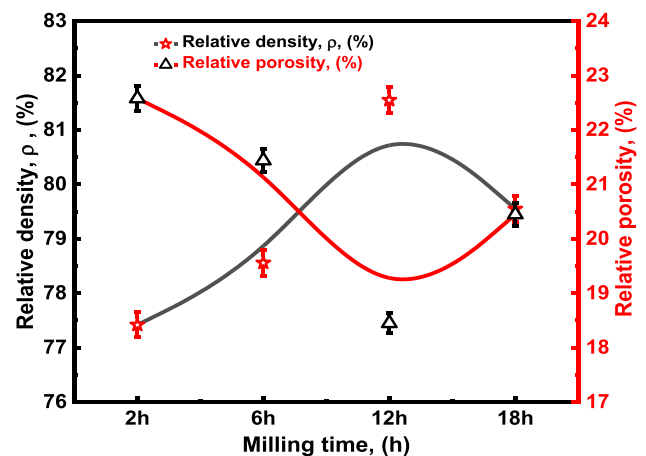

Fig. 15 Evolution of the relative porosity; (%) and the relative density; (%) versus milling time (2, 6, 12, and 18 h) of sintered Ti-25Nb-25Mo samples

less than 10 μm, and the pores exhibited a greater degree of uniformity in size. This is a result of the mechanical alloying process's blending, homogenization, and grain size refining.

Figure 16 indicates that both porosity and mean pore size of Ti-25Nb-25Mo are decreased with increasing milling time (2–12 h). This is due to the refinement of the grain size resulting from the mechanical alloying procedure [65].

The pore size decreases with increasing milling time, this conclusion has also been reported by Kim et al. [20], for 4, 8, and 12 h of milling time. The larger pores observed for samples

with a high milling time (18 h) may be due to the agglomeration of many pores during the sintering process [61].

3.2.3 Microhardness and modulus of elasticity properties

Figure 17 illustrates the results of microhardness testing conducted on Ti-25Nb-25Mo alloys that were milled for durations ranging from 2 to 18 h. The results indicate that there was an increase in microhardness as the milling time increased (2–12 h), which subsequently decreased after 18 h
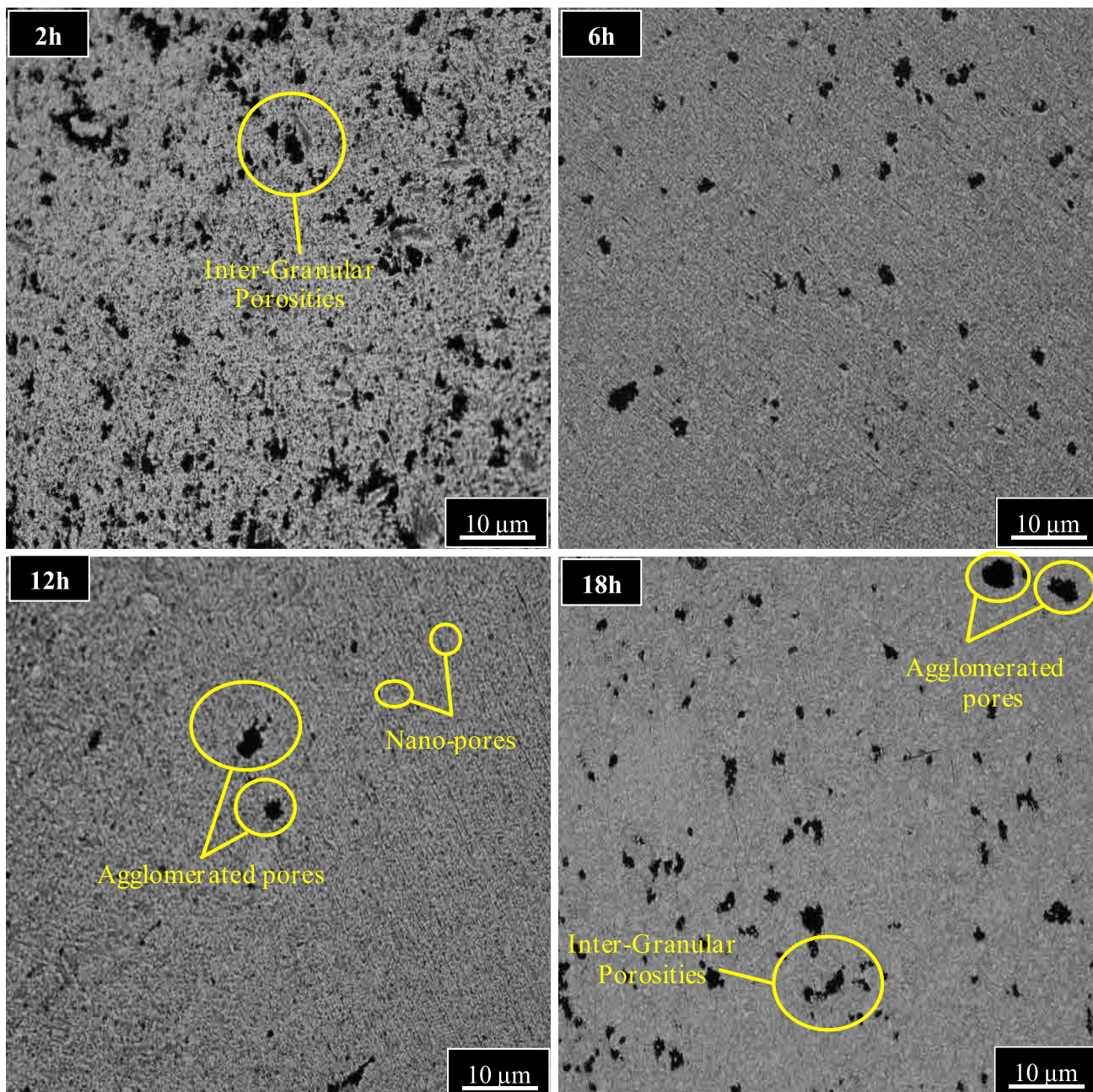

Fig. 16 Optical microscopy micrographs of porosity and pore size distribution of sintered and milled Ti-25Nb-25Mo for variable durations
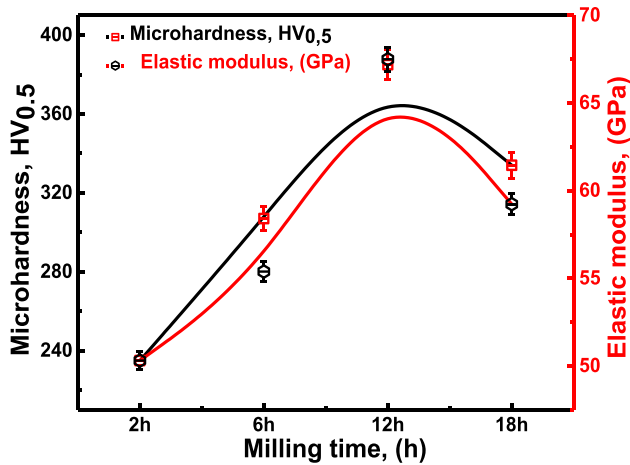
Fig. 17 Vickers hardness values and elastic modulus evolution of milled and sintered Ti-25Nb-25Mo system at different milling time for: 2, 6, 12, and 18 h

of milling. The highest microhardness value of 385 $HV_{0.5}$ was achieved after 12 h of milling, while the lowest value of 235 $HV_{0.5}$ was obtained after 2 h of milling. It should be noted that the reduction in crystallite size played a significant role in the observed increase in the microhardness of the titanium alloys. This is because grain size refinement leads to a strengthening mechanism that contributes to the overall hardness of the material. Furthermore, a correlation was established between the porosity and the hardness, indicating that an increase in the number of pores corresponded to a decrease in the hardness value [26].

Figure 17 also displays the elastic modulus of the Ti-25Nb-25Mo specimens, which were assessed and recorded with milling time varying from 2 to 18 h. The Young modulus of the ternary alloy increased from 50 to 68 GPa with increasing milling times to achieve the highest value at 12 h similar to hardness tendency.

The physical characteristics of the samples were enhanced as the milling time increased. Specifically, Ti-10Mo-(3, 7, 10)Nb alloys are promising choices in biomedical applications due to their combination of high strength and low elastic modulus [22].

According to Xu et al.'s study [22], the Ti-Mo-Nb system demonstrated superior mechanical characteristics such as higher Vickers microhardness values (ranging from 394 to 441 HV), increased compression strength and yield strength, substantial plastic strain capacity, and a low elastic modulus (ranging from 24.7 to 28.4 GPa), which is comparable to the Young modulus of bone.

The mechanical characteristics are highly affected by the amount of porosity, pore size, shape, and distribution. Additionally, chemical composition and grain size are the main factors that can affect the mechanical characteristics of alloys such as microhardness and elastic modulus.

The hardness of Ti-Nb-Mo samples were higher than that of pure titanium, which can be attributed to the solid solution strengthening mechanism and the presence of a fine microstructure. Porosity determines the mechanical properties of Ti-25Nb-25Mo samples, especially the Young modulus [16]. Because an optimal porosity level enables the creation of titanium alloys that exhibit both low Young's modulus and high strength [27].

Figure 18 represents the H/E and H^3/E^2 proportions of Ti-25Nb-25Mo alloys at different milling time. It has been observed that the H/E values increase from 0.046 at 2 h of milling to 0.056 at 12 h of milling, and then decrease to 0.055 at 18 h of milling time. This variation demonstrates that as milling time increases, the alloy's wear resistance increases initially, but eventually decreases. Actually, the Ti-25Nb-25Mo sample milled for 12 h exhibits the highest H/E value of 0.056, indicating that the alloy is wear resistant [33, 66].

One other variable (H^3/E^2) implies plastic deformation resistance; a larger value of the H^3/E^2 represents the higher resistance to plastic deformation [33, 66, 67]. Because wear is the progressive loss of material resulting from plastic deformation, this H^3/E^2 variable could reveal a material's anti-wear ability [33, 67]. Indeed, the high value of H^3/E^2 indicates a long service life [33, 67, 68]. The H^3/E^2 values have the identical varying tendency as H/E values. The H^3/E^2 values increase from 0.0048 GPa to 0.0118 GPa from 2 to 12 h of milling time respectively and then decrease to 0.01 GPa at 18 h of milling time. Therefore, the Ti-25Nb-25Mo (milled at 12 h) with the larger H^3/E^2 value in current Ti-Nb-Mo alloys suggests excellent anti-wear properties.

In addition, the H/E and the H^3/E^2 values of three Ti-25Nb-25Mo samples milled at 2, 6, 12, and 18 h are higher than those of the commercially pure titanium (0.024 and 0.0014 GPa, respectively) and are comparable to the H/E and H^3/E^2 values of Ti-Fe and Ti-Fe-Ta alloys [33,
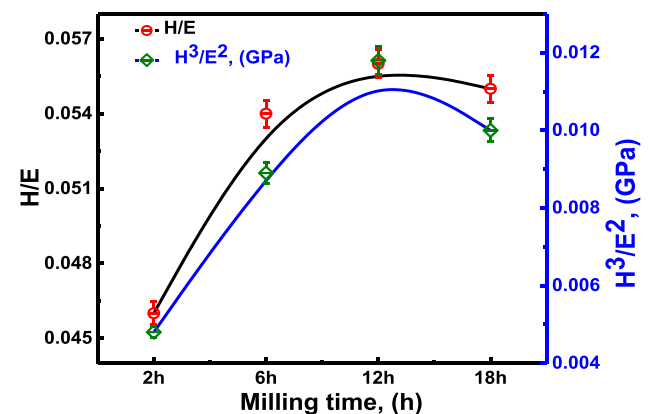

Fig. 18 The mechanical characteristics (H/E, and H^3/E^2) variation of milled and sintered Ti-25Nb-25Mo specimens at different milling time (2, 6, 12, and 18 h)

Table 3 Determined hardness, elastic modulus, H/E, and H^3/E^2 values of Ti-25Nb-25Mo specimens at varying milling times (2–18 h)
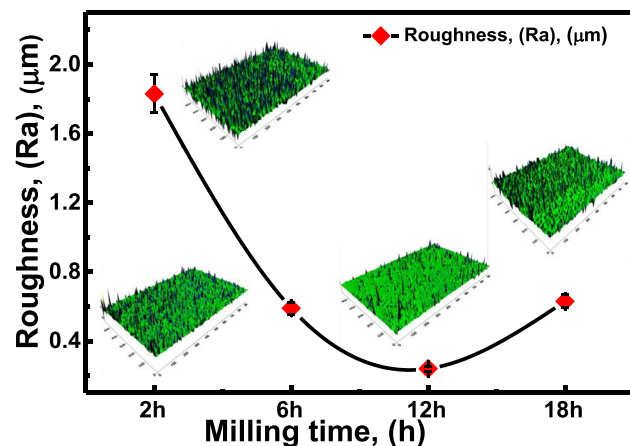
Milling time (h)	H (HV$_{0.5}$)	H (GPa)	E (GPa)	H/E	H^3/E^2 (GPa)
2	235	2.305	50.31	0.046	0.0048
6	307	3.011	55.39	0.054	0.0089
12	385	3.776	67.50	0.056	0.0118
18	334	3.276	59.23	0.055	0.0100

Table 4 Surface roughness parameters of sintered Ti-25Nb-25Mo alloy after milling process for: 2, 6, 12, and 18 h

Milling time	R_a (µm)	R_t (µm)	R_q (µm)	R_z (µm)
2 h	1.83	25.47	2.71	11.22
6 h	0.59	8.34	0.98	5.06
12 h	0.24	2.73	0.33	1.28
18 h	0.63	3.71	0.79	2.86

where: R_a Average Roughness, R_q Root Mean Squared (RMS) Roughness, R_t Peak to Valley Height, and R_z Roughness Depth

67], signifying that Ti-25Nb-25Mo alloys are resistant to wear and possess the capability to function as biomedical materials for an extended period [33] (Table 3).

3.2.4 Roughness analysis

Figure 19 displays the Ti-25Nb-25Mo alloy's roughness (Ra) evolution in relation to milling time. The roughness of the alloy samples was significantly impacted by the duration of the milling process. According to the findings, the roughness exhibited a decreasing trend when the milling time increased, from a value of 1.83 µm to a value of 0.24 µm at milling times of 2 and 12 h, respectively. This can be attributed to the particles increased hardness and fineness during the milling process (Fig. 19).

The morphology and propagation of cells are significantly affected by surface roughness. Tissue growth and biocompatibility benefit from rougher topography. Furthermore, the presence of micro-pores in a bone structure mitigates stress-shielding effects, promoting beneficial tissue growth that facilitates fibroblast penetration into the implant and supports the generation of fresh tissue within it. Flat implant surfaces, conversely, hinder opportune cells from adhering, limiting overall biocompatibility [61]. According to the literature, increased surface roughness can enhance

the amount of cells attaching to the substrate leading to an increased cellular activity [69–73] (Table 4).

4 Conclusions

The findings of our research on the milling time effect on microstructural evolution, and mechanical behavior of the Ti-25Nb-25Mo alloy system are quite convincing, and from the outcomes, it is possible to conclude that:

- The sintered Ti25Nb-25Mo alloys produced from powders milled at 12 h exhibited fine grain size and uniform distribution of additional elements (Nb and Mo).
- The average pore size decreased as milling time increased. The Ti-25Nb-25Mo samples, which were sintered from powders milled at 12, and 18 h, presented the smallest mean pore size.
- Milling time has an impact on biomaterials' functionality and compatibility with cells and tissues by their effect on surface roughness, a critical parameter.
- The relative density, microhardness, and elastic modulus were increased with milling time. Owing to the low porosity and ultrafine grain structure, an increase in milling time significantly improved the microhardness, density, and roughness of the Ti-25Nb-25Mo alloy.
- Reduced porosity, increased density, and hardness were the main factors in reducing wear rate. This is due to the improved microstructural and mechanical characteristics of the samples after 12, and 18 h of milling.
- The mechanical properties and wear behavior of the Ti-25Nb-25Mo samples were influenced by grain size, surface roughness, and surface texture. The Ti-25Nb-25Mo alloy can be used in bone implants due to its excellent structural and mechanical characteristics.
- Increasing the milling duration resulted in enhanced mechanical characteristics values (H/E and H^3/E^2), thereby leading to improved anti-wear ability and greater resistance to plastic deformation in the Ti-25Nb-25Mo alloy.
- Ti-Nb-Mo alloys, milled for 12, and 18 h, are largely satisfied the imposed requirements for the selection of biomedical implant applications.

Fig. 19 Roughness < Ra >, (µm) evolution of sintered Ti-25Nb-25Mo alloy after milling process (2, 6, 12, and 18 h)

Data availability 'Not Applicable'.

Declarations

Ethical approval 'Not Applicable'.

Conflict of interest The authors have no conflicts to disclose.

References

1. Affatato S, Ruggiero A, Merola M (2015) Advanced biomaterials in hip joint arthroplasty. A review on polymer and ceramics composites as alternative bearings. Compos Part B: Eng 83:276–283

2. Shan L, Shan B, Graham D, Saxena A (2014) Total hip replacement: a systematic review and meta-analysis on mid-term quality of life. Osteoarthritis Cartilage 22(3):389–406

3. Hu CY, Yoon TR (2018) Recent updates for biomaterials used in total hip arthroplasty. Biomater Res 22(1):1–12

4. Rabiei A (2021) Hip Prostheses. Biomed Mater 517–535

5. Merola M, Affatato S (2019) Materials for hip prostheses: a review of wear and loading considerations. Materials 12(3):495

6. Guo L, Naghavi SA, Wang Z, Varma SN, Han Z, Yao Z, Liu C (2022) On the design evolution of hip implants: A review. Mater Des 216:110552

7. Xu W, Lu X, Tian J, Huang C, Chen M, Yan Y, ... Wen C (2020) Microstructure, wear resistance, and corrosion performance of Ti35Zr28Nb alloy fabricated by powder metallurgy for orthopedic applications. J Mater Sci Technol 41:191–198.

8. Shankar S, Nithyaprakash R, Abbas G (2021) Tribological Study on Titanium Based Composite Materials in Biomedical Applications. Tribological Appl Compos Mater 215–241

9. Hybasek V, Fojt J, Malek J, Jablonska E, Pruchova E, Joska L, Ruml T (2020) Mechanical properties, corrosion behaviour and biocompatibility of TiNbTaSn for dentistry. Mater Res Express 7(1):015403

10. Xu W, Lu X, Wang LN, Shi ZM, Lv SM, Qian M, Qu XH (2018) Mechanical properties, in vitro corrosion resistance and biocompatibility of metal injection molded Ti-12Mo alloy for dental applications. J Mech Behav Biomed Mater 88:534–547

11. Campos-Quirós A, Cubero-Sesín JM, Edalati K (2020) Synthesis of nanostructured biomaterials by high-pressure torsion: Effect of niobium content on microstructure and mechanical properties of Ti-Nb alloys. Mater Sci Eng, A 795:139972

12. Xu W, Chen M, Lu X, Zhang DW, Singh HP, Jian-shu Y, ... Liu CZ (2020) Effects of Mo content on corrosion and tribocorrosion behaviours of Ti-Mo orthopaedic alloys fabricated by powder metallurgy. Corros Sci 168:108557

13. Niinomi M, Nakai M (2019) Ti-based biomedical alloys. Novel Structured Metallic and Inorganic Materials 61–76

14. Chui P, Jing R, Zhang F, Li J, Feng T (2020) Mechanical properties and corrosion behavior of β-type Ti-Zr-Nb-Mo alloys for biomedical application. J Alloy Compd 842:155693

15. Biesiekierski A, Lin J, Munir K, Ozan S, Li Y, Wen C (2018) An investigation of the mechanical and microstructural evolution of a TiNbZr alloy with varied aging time. Sci Rep 8(1):1–12

16. Adamek G, Junka A, Wirstlein P, Jurczyk MU, Siwak P, Koper J, Jakubowicz J (2022) Biomedical Ti-Nb-Zr Foams Prepared by Means of Thermal Dealloying Process and Electrochemical Modification. Materials 15(6):2130

17. Xu W, Tian J, Liu Z, Lu X, Hayat MD, Yan Y, ... Wen C (2019) Novel porous Ti35Zr28Nb scaffolds fabricated by powder metallurgy with excellent osteointegration ability for bone-tissue engineering applications. Mater Sci Eng: C 105:110015

18. Yan XH, Ma J, Zhang Y (2019) High-throughput screening for biomedical applications in a Ti-Zr-Nb alloy system through masking co-sputtering. Sci China Phys Mech Astron 62(9):1–9

19. Fatichi AZ, Mello MG, Caram R, Cremasco A (2019) Self-organized TiO2 nanotube layer on Ti–Nb–Zr alloys: Growth, characterization, and effect on corrosion behavior. J Appl Electrochem 49(11):1079–1089

20. Kim DG, Woo KD, Kang DS, Lee T (2014) Effect of Milling Time on Pore Size and Distribution of Ti-Nb-Zr Biomaterials with Space Holder Consolidated by Spark Plasma Sintering. Korean J Mater Res 24(2):111–115

21. Li H, Cai Q, Li S, Xu H (2022) Effects of Mo equivalent on the phase constituent, microstructure and compressive mechanical properties of Ti–Nb–Mo–Ta alloys prepared by powder metallurgy. J Market Res 16:588–598

22. Xu LJ, Chen YY, Liu ZG, Kong FT (2008) The microstructure and properties of Ti–Mo–Nb alloys for biomedical application. J Alloy Compd 453(1–2):320–324

23. Dinu M, Franchi S, Pruna V, Cotrut CM, Secchi V, Santi M, ... Vladescu A (2018) Ti-Nb-Zr system and its surface biofunctionalization for biomedical applications. In Titanium in Medical and Dental Applications. Woodhead Publishing 175–200

24. da Silva FL, Antonini LM, Vega MRO, Aguzzoli C, de Malfatti-Fraga C (2020) A New Ternary Alloy Ti26Zr24Nb for Biomedical Application: Behavior in Corrosion, Wear, and Tribocorrosion. J Bio- Tribo-Corros 6(3):1–13

25. Neacsu P, Gordin DM, Mitran V, Gloriant T, Costache M, Cimpean A (2015) In vitro performance assessment of new beta Ti–Mo–Nb alloy compositions. Mater Sci Eng, C 47:105–113

26. Fellah M, Hezil N, Touhami MZ, AbdulSamad M, Obrosov A, Bokov DO, ... Alhussein A (2020) Structural, tribological and antibacterial properties of (α+ β) based ti-alloys for biomedical applications. J Mater Res Technol 9(6):14061–14074

27. Sochacka P, Miklaszewski A, Jurczyk M (2019) Development of β-type Ti-x at.% Mo alloys by mechanical alloying and powder metallurgy: Phase evolution and mechanical properties (10≤ x≤ 35). J Alloys Compd 776:370–378

28. Gouvea EDS, Rossi MC, Escuder AV, Afonso CRM, Borrás VA (2022) Relation between Mechanical Milling Parameters in Phase Transformation and Oxygen Content in Ti–Nb–Mo Powders for Posterior Sintering. Metals 12(8):1238

29. Salvo C, Aguilar C, Cardoso-Gil R, Medina A, Bejar L, Mangalaraja RV (2017) Study on the microstructural evolution of Ti-Nb based alloy obtained by high-energy ball milling. J Alloy Compd 720:254–263

30. Mendes MW, Ágreda CG, Bressiani AH, Bressiani JC (2016) A new titanium based alloy Ti–27Nb–13Zr produced by powder metallurgy with biomimetic coating for use as a biomaterial. Mater Sci Eng, C 63:671–677

31. Fellah M, Hezil N, Touhami MZ, Obrosov A, Weiß S, Kashkarov EB, ... Iost A (2019) Enhanced structural and tribological performance of nanostructured Ti–15Nb alloy for biomedical applications. Results Phys 15 :102767.

32. Fellah M, Hezil N, Abdul Samad M, Djellabi R, Montagne A, Mejias A, ... Weiss S (2019) Effect of Molybdenum content on structural, mechanical, and tribological properties of hot isostatically pressed β-type titanium alloys for orthopedic applications. J Mater Eng Perform 28(10) :5988–5999

33. Li P, Ma X, Tong T, Wang Y (2020) Microstructural and mechanical properties of β-type Ti–Mo–Nb biomedical alloys with low elastic modulus. J Alloy Compd 815:152412

34. Fellah M, Hezil N, Hussein MA, Samad MA, Touhami MZ, Montagne A, ... Weiss S (2019) Preliminary investigation on the bio-tribocorrosion behavior of porous nanostructured β-type titanium based biomedical alloys. Mater Lett 257:126755

35. Kong Q, Lai X, An X, Feng W, Lu C, Wu J, ... Wang Q (2020) Characterization and corrosion behaviour of Ti-13Nb-13Zr alloy prepared by mechanical alloying and spark plasma sintering. Mater Today Commun 23:101130

36. Hussein M, Adesina AY, Kumar M, Azeem M, Sorour A, Nasser AA (2021) Improvement of in vitro corrosion, wear, and mechanical properties of newly developed Ti alloy by thermal treatment for dental applications. Trans Nonferrous Met Soc China 31(4):952–966

37. Kalita D, Rogal Ł, Berent K, Góral A, Dutkiewicz J (2021) Effect of Mo and Ta on the mechanical and superelastic properties of Ti-Nb alloys prepared by mechanical alloying and spark plasma sintering. Materials 14(10):2619

38. Oshida Y (2010) Bioscience and bioengineering of titanium materials. Elsevier

39. Ishiyama S, Hanada S, Izumi O (1991) Effect of Zr, Sn and Al additions on deformation mode and beta phase stability of metastable beta Ti alloys. ISIJ Int 31(8):807–813

40. Hao YL, Li SJ, Sun SY, Yang R (2006) Effect of Zr and Sn on Young's modulus and superelasticity of Ti–Nb-based alloys. Mater Sci Eng, A 441(1–2):112–118

41. Niinomi M, Nakai M, Hieda J (2012) Development of new metallic alloys for biomedical applications. Acta Biomater 8(11):3888–3903

42. Cardoso GC, de Almeida GS, Corrêa DOG, Zambuzzi WF, Buzalaf MAR, Correa DRN, Grandini CR (2022) Preparation and characterization of novel as-cast Ti-Mo-Nb alloys for biomedical applications. Sci Rep 12(1):1–9

43. Nnamchi PS, Obayi CS, Todd I, Rainforth MW (2016) Mechanical and electrochemical characterisation of new Ti–Mo–Nb–Zr alloys for biomedical applications. J Mech Behav Biomed Mater 60:68–77

44 Martienssen W, Warlimont H (eds) (2006) Springer handbook of condensed matter and materials data. Springer Science & Business Media

45. Li H, Cai Q, Liu J, Feng X, Li S (2021) Effects of Nb and Mo content on mechanical properties of Ti-Nb-Mo-Ta alloys by two-step pressure-free and hot isostatic pressing sintering. J Phys: Conf Ser IOP Publ 1965(1):012114

46. Suryanarayana C (2019) Mechanical alloying: a novel technique to synthesize advanced materials. Research 2019:1–17

47. Fellah M, Hezil N, Dekhil L, Abdul Samad M, Djellabi R, Kosman S, Montagne A, Iost A, Obrosov A, Weiss S (2019) Effect of sintering temperature on structure and tribological properties of nanostructured Ti−15Mo alloy for biomedical applications. Trans Nonferrous Met Soc China 29(11):2310–2320

48. W H eq Yang M, Guo Z, Xiong J, Liu F, Qi K (2017) Microstructural changes of (Ti, W) C solid solution induced by ball milling. Int J Refract Met Hard Mater 66:83–87

49. Wang H, Ban C, Zhao N, Kang Y, Qin T, Liu S, Cui J (2020) Enhanced strength and ductility of nano-grained titanium processed by two-step severe plastic deformation. Mater Lett 266:127485

50. ISO EN (1997) 4287–Geometrical Product Specifications (GPS)–Surface Texture: Profile Method–Terms, Definitions and Surface Texture Parameters. International Organization for Standardization: Geneva, Switzerland

51. Alves AK (2021) Technological Applications of Nanomaterials. Springer, Switzerland

52. Shaterabadi Z, Nabiyouni G, Soleymani M (2018) Optimal size for heating efficiency of superparamagnetic dextran-coated magnetite nanoparticles for application in magnetic fluid hyperthermia. Physica C: Supercond Appl 549:84–87

53. Omran AN, Ali MM, Kh MM (2020) Biocompatibility, corrosion, and wear resistance of β titanium alloys for biomedical applications. Appl Phys A 126(12):1–12

54. Al-Aqeeli N, Hussein MA, Suryanarayana C (2015) Phase evolution during high energy ball milling of immiscible Nb–Zr alloys. Adv Powder Technol 26(2):385–391

55. Baker H, Okamoto H (1992) ASM handbook. vol 3. alloy phase diagrams. ASM International, Materials Park, Ohio 44073–0002, USA 1992, 501

56. Craver CD (ed) (1982) The Coblentz Society. The Coblentz Society desk book of infrared spectra

57. Smith AL (1982) The Coblentz Society Desk Book of Infrared Spectra in Carver, C.D., editor, The Coblentz Society Desk Book of Infrared Spectra, Second Edition, The Coblentz Society: Kirkwood, MO 1–24

58. Maheswari N, Muralidharan G (2017) Controlled synthesis of nanostructured molybdenum oxide electrodes for high-performance supercapacitor devices. Appl Surf Sci 416:461–469

59. Essalah G, Guermazi H, Guermazi S, Leroy G, Duponchel B, Mascot M, ... Mangavati S (2022) Enhanced dielectric properties of ternary ZnO-based composites for dielectric applications. Appl Phys A 128:1–12

60. Atta AA, Hassanien AM, El-Nahass MM, Shaltout AA, Al-Talhi YA, Aljoudi AM (2019) Influence of argon flow rate on structural and optical properties of transparent Nb 2 O 5 thin films. Opt Quant Electron 51:1–17

61. Fouzia H, Mamoun F, Naouel H, Linda A, Goussem M, Said M, ... Obrosov A (2021) The effect of milling time on the microstructure and mechanical properties of Ti-6Al-4Fe alloys. Mater Today Commun 27:102428

62. Fellah M, Hezil N, Bouras D, Montagne A, Obrosov A, Ibrahim RW, Iqbal A, El Din S, Abd El-WahedKhalifa H (2023) Investigating the effect of milling time on structural, mechanical and tribological properties of a nanostructured hiped alpha alumina for biomaterial applications. Arabian J Chem 16(10):105112

63. Long Y, Zhang H, Wang T, Huang X, Li Y, Wu J, Chen H (2013) High-strength Ti–6Al–4V with ultrafine-grained structure fabricated by high energy ball milling and spark plasma sintering. Mater Sci Eng, A 585:408–414

64. Behera A, Behera A (2022) Nanomaterials. Advanced Materials: An Introduction to Modern Materials Science 77–125

65. Mamoun F, Hezil N, Bouras D, Obrosov A, Mohammed AS, Montagne A, ... Weiß S (2023) Structural, Mechanical and Tribological Performance of a nano structured Biomaterial Co-Cr-Mo Alloy Synthesized Via Mechanical Alloying. J Mater Res Technol 25:2152–2165

66. Hezil N, Aissani L, Fellah M, Samad MA, Obrosov A, Timofei C, Marchenko E (2022) Structural, and tribological properties of nanostructured α+ β type titanium alloys for total hip. J Market Res 19:3568–3578

67. Musil J, Kunc F, Zeman H, Polakova H (2002) Relationships between hardness, Young's modulus and elastic recovery in hard nanocomposite coatings. Surf Coat Technol 154(2–3):304–313

68. Xu J, dong Wang G, Lu X, Liu L, Munroe P, Xie ZH (2014) Mechanical and corrosion-resistant properties of Ti–Nb–Si–N nanocomposite films prepared by a double glow discharge plasma technique. Ceram Int 40(6):8621-8630

69. Jeong YH, Son IB, Choe HC (2011) Formation of surface roughness on the Ti-35Nb-xZr alloy using femtosecond laser for biocompatibility. Procedia Eng 10:2393–2398

70. Hezil N, Fellah M (2019) Synthesis and structural and mechanical properties of nanobioceramic (α-Al2O3). J Aust Ceram Soc 55(4):1167–1175

71. Dekhil L, Hanneche N, Fellah M, Bououdina M, Mercier AM (2020) Structural analysis and densification study of the mechanically alloyed Cr 50 Ni 50 powders. Int J Adv Manuf Technol 108:2515–2524

72. Fellah M, Samad MA, Labaiz M, Assala O, Iost A (2015) Sliding friction and wear performance of the nano-bioceramic α-Al2O3 prepared by high energy milling. Tribol Int 91:151–159

73. Bougoffa MSE, Bachirbey MN, Benouali C, Sayah T, Fellah M, Abdul Samad M (2021) Dry Sliding friction and wear behavior of CuZn39Pb2 and AA7075 under industrial and laboratory conditions. J Bio- Tribo-Corros 7:1–17

Publisher's Note Springer Nature remains neutral with regard to jurisdictional claims in published maps and institutional affiliations.